

## THE EFFECTS OF POLARIZED FOREGROUNDS ON 21 cm EPOCH OF REIONIZATION POWER SPECTRUM MEASUREMENTS

DAVID F. MOORE<sup>1</sup>, JAMES E. AGUIRRE<sup>1</sup>, AARON R. PARSONS<sup>2</sup>, DANIEL C. JACOBS<sup>3</sup>, AND JONATHAN C. POBER<sup>2</sup>

ACCEPTED TO APJ: 2013 April 21

### ABSTRACT

Experiments aimed at detecting highly-redshifted 21 centimeter emission from the Epoch of Reionization (EoR) are plagued by the contamination of foreground emission. A potentially important source of contaminating foregrounds may be Faraday-rotated, polarized emission, which leaks into the estimate of the intrinsically unpolarized EoR signal. While these foregrounds' intrinsic polarization may not be problematic, the spectral structure introduced by the Faraday rotation could be. To better understand and characterize these effects, we present a simulation of the polarized sky between 120 and 180 MHz. We compute a single visibility, and estimate the three-dimensional power spectrum from that visibility using the delay spectrum approach presented in Parsons et al. (2012b). Using the Donald C. Backer Precision Array to Probe the Epoch of Reionization (PAPER) as an example instrument, we show the expected leakage into the unpolarized power spectrum to be several orders of magnitude above the expected 21cm EoR signal.

*Subject headings:* cosmology: observations – instrumentation: interferometers – instrumentation: polarization

### 1. INTRODUCTION

A significant amount of thought has gone into the problem of foreground removal allowing for the detection of the power spectrum of neutral hydrogen during the Epoch of Reionization (EoR) (Bowman et al. 2009; Morales et al. 2006; Liu et al. 2009; Liu & Tegmark 2011; Dillon et al. 2013, e.g.). Essential to nearly all these techniques is the spectral smoothness of these foregrounds, which allows for a separation in  $k$  space of the foreground emission and the signal from the EoR. Various mechanisms will leak polarized emission into the best estimate of the EoR signal, which then may introduce spectral structure to an EoR experiment's measurement.

By contrast to unpolarized foregrounds, comparatively little work has addressed the problem of detecting and removing polarized foregrounds. Pen et al. (2009) provided some of the first relevant upper limits at small angular scales using the Giant Metre-Wave Telescope (GMRT). They found, for spherical harmonic multipoles  $200 \leq \ell \leq 5000$ , an angular power spectrum upper limit of around  $C_\ell \lesssim 100 \text{ mK}^2$ . More recent work by Bernardi et al. (2010) detected polarized power at the same level at  $\ell \lesssim 1000$  using the Westerbork Synthesis Radio Telescope (WSRT), with no significant detection above  $\ell$  of 1000. Bernardi et al. (2010) did not detect emission directly attributable to polarized point sources. Pen et al. (2009) present their upper limit in terms of the three-dimensional power spectrum, but Bernardi et al. (2010) only present a  $C_\ell$  spectrum which has been integrated along the frequency direction. Figure 1 gives a summary of the low-frequency measurements of polarized power spectra. It is clear that the angular power spectrum of the unpolarized sky must be scaled by a

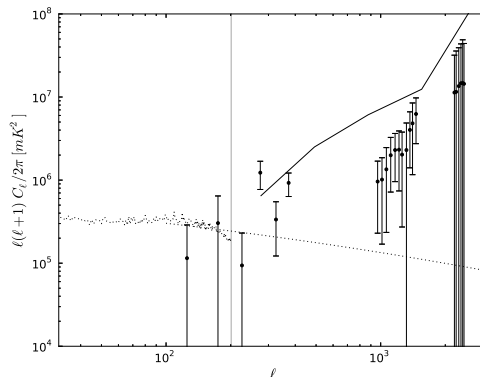


FIG. 1.— Recent estimates of low-frequency polarized power spectra. The thick black points with error bars show the Bernardi et al. (2010) measurements of a field around 3C196, and the solid line shows the upper limit of Pen et al. (2009). The Haslam map at 408 MHz (Haslam et al. 1982), scaled by a polarization fraction of 0.3%, is shown by thin points, and a power-law extrapolation is shown with a dotted line above  $\ell = 200$ . This fraction was chosen to agree with the low- $\ell$  points in the Bernardi measurement. At high- $\ell$ , the upper limits do not constrain the level of polarized emission. The grey vertical line shows the  $\ell$  mode sampled by the simulation in this paper, as a point of reference.

mean polarization fraction of about 0.3% to agree with the Bernardi et al. (2010) measurements. This requires a significant degree of depolarization of synchrotron emission from ordered magnetic fields.

Jelić et al. (2010) attempted to further constrain the problem by fully simulating a full-Stokes realization of galactic synchrotron emission over a  $10^\circ \times 10^\circ$  field of view. They present a realistic spectrum of the mean temperature of polarized emission, but do not extend their analysis into the power spectrum. Their analysis also predicts a polarization fraction from diffuse emission much higher than the limited measurements available. Geil et al. (2011) also investigate the issue, proposing the use of the RMCLEAN algorithm (Heald et al. 2009) to

<sup>1</sup> Dept. of Physics and Astronomy, U. Pennsylvania, Philadelphia, PA, damo@sas.upenn.edu

<sup>2</sup> Astronomy Dept. U. California, Berkeley, CA

<sup>3</sup> School of Earth and Space Exploration, Arizona State U., Tempe, AZ

mitigate the effects of these polarized foregrounds. While these papers provide detailed descriptions of the polarized sky and removal strategies in the image plane, they provide little discussion of the line-of-sight direction.

This paper aims to steer the discussion of polarized foregrounds towards the *terra incognita* of the third, frequency dimension. We begin in section 2 reviewing the basics of polarized interferometry, and the delay spectrum approach to estimating the power spectrum, presented in Parsons et al. (2012b). We discuss the relevance of polarized foregrounds to measuring the 21cm power spectrum. In section 3, we discuss the design and implementation of a simulation of the polarized sky and its results. Finally, in section 4 we briefly discuss prospects of polarized source removal and leakage mitigation.

Throughout the paper, we will use the Donald C. Backer Precision Array to Probe the Epoch of Reionization (PAPER)(Parsons et al. 2010) as a model instrument. The results are not specific to that instrument, nor are they specific to the Delay Spectrum analysis used in this paper (Parsons et al. 2012b). Any 21cm EoR power spectrum detection experiment with linear feeds, including the Murchison Widefield Array (Tingay et al. 2013) or the Low Frequency ARray (Röttgering 2003) could fall subject to the leakages described here without a perfect calibration.

## 2. PRELIMINARIES

### 2.1. Definition of Stokes Visibilities

Two prominent ways in which polarized sky emission can leak into an interferometric estimate of Stokes  $I$  are leakages due to non-orthogonal and rotated feeds and beam ellipticity — an asymmetry in the two linear polarizations of a primary beam which causes unpolarized signals to appear polarized, and vice versa. The first is a well-understood question, discussed in length in the series of papers by Hamaker et al. (1996). This type of leakage can be corrected by the proper linear combination of visibilities. Hence, we will focus on the latter issue. To begin, we will examine the contents of an interferometric spectrum, and relate them to the intrinsic Stokes parameters.

As a reminder, we present the measurement equation for an interferometer in the flat-sky limit:

$$\mathcal{V}_{ab}(u, v, \nu) = \int A_{ab}(l, m) I_{ab}(l, m) e^{-2\pi i(uv+lm)} dldm. \quad (1)$$

Here the polarization indices  $a, b$  indicate the polarization state of the measurement.  $A_{ab}$  is the primary beam,  $l$  and  $m$  are direction cosines of the celestial sphere (with their Fourier components  $u$  and  $v$ ), and  $I_{ab}$  is the sky emission projected along the polarization state of the measurement. Henceforth, we will be writing all visibility equations in the flat-sky limit. We can do this without loss of generality since the polarization properties of a visibility are unaffected by this assumption.

It is worth noting that each linear feed measures a one-dimensional projection of the incident electric field. This causes correlations with different feed orientations to contain information about different polarization states of the incident radiation. A convenient short-hand notation for the polarization content of each visibility is

$$\begin{pmatrix} \mathcal{V}_{xx} & \mathcal{V}_{xy} \\ \mathcal{V}_{yx} & \mathcal{V}_{yy} \end{pmatrix}_{ij} = \mathbf{J}_i \cdot \begin{pmatrix} I + Q & U - iV \\ U + iV & I - Q \end{pmatrix} \cdot \mathbf{J}_j^\dagger \quad (2)$$

The Jones matrices  $\mathbf{J}_{i,j}$  (see Hamaker et al. 1996) relate the sky emission ( $I$ ,  $Q$ ,  $U$ , and  $V$ ) to an interferometric measurement. Each antenna's Jones matrix is dependent on nearly all instrumental parameters, but for the purposes of this paper, we will investigate the effects of direction-dependent gains, or the primary beam.

In the flat-sky approximation, an interferometer natively measures the two-dimensional spatial Fourier transform of the sky. Ideally, this would allow an observer to estimate the three-dimensional power spectrum by simply transforming the frequency, line of sight direction, and cross-multiplying measurements without imaging. Relaxing the imaging requirement provides an incentive to make estimates of the Stokes parameters —  $I$  for instance — in the visibility domain, where the Stokes parameters are not defined. A naïve addition between the linearly polarized,  $xx$  and  $yy$  visibilities should estimate the total power of sky emission, Stokes  $I$ . Similar operations can be performed for all polarization states. A sensible method of estimating the four Stokes parameters in the visibility domain is to add visibilities as images are typically added. Hence, we define Stokes visibilities (for linear feeds) as:

$$\begin{pmatrix} \mathcal{V}_I \\ \mathcal{V}_Q \\ \mathcal{V}_U \\ \mathcal{V}_V \end{pmatrix} \equiv \frac{1}{2} \begin{pmatrix} 1 & 0 & 0 & 1 \\ 1 & 0 & 0 & -1 \\ 0 & 1 & 1 & 0 \\ 0 & i & -i & 0 \end{pmatrix} \begin{pmatrix} \mathcal{V}_{xx} \\ \mathcal{V}_{xy} \\ \mathcal{V}_{yx} \\ \mathcal{V}_{yy} \end{pmatrix}. \quad (3)$$

Explicitly writing the expression of  $\mathcal{V}_I$  by substituting equation 1 into equation 3, we find that

$$\begin{aligned} \mathcal{V}_I &= \mathcal{V}_{xx} + \mathcal{V}_{yy} \\ &= \int (A_{xx} + A_{yy}) I e^{-2\pi i(lu+vm)} dldm \\ &\quad + \int (A_{xx} - A_{yy}) Q e^{-2\pi i(lu+vm)} dldm. \end{aligned} \quad (4)$$

Writing the visibility this way highlights one source of polarized leakage: that due to beam ellipticity. If the  $xx$  and  $yy$  beams are not equal, the last term of the equation 4 would be non-zero. Polarized emission then enters the estimate of  $I$ , weighted by the differenced beam. This equation also points out the difference between Stokes parameters and the Stokes visibilities defined in equation 3. They estimate their respective Stokes parameters, but still include terms from other polarization states.

Thus, if an instrument's linearly polarized beam is not symmetric under a 90° rotation, all the intrinsic linear polarization will not cancel, corrupting the visibility estimate of Stokes parameters. Figure 2 shows two slices through the model beam for PAPER, through constant azimuth and through zenith, and a cut through the same beam, rotated by 90°. We note that these slices are not identical, and show the differenced beam, which provides the mechanism for leakage.

In an image-based analysis, these effects may be corrected by a simple re-weighting of the image, but these reconstructions are subject to the accuracy of the primary beam model. The results of this paper indicate

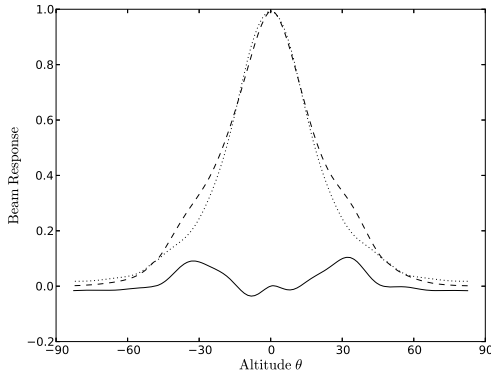


FIG. 2.— Power vs. altitude through zenith for east-west slices of the  $xx$  and  $yy$  PAPER beams (dashed, dotted respectively). The solid line shows their difference.

the leakages due to the primary beam shown in figure 2, but could equally be applied to an image-based analysis whose primary beam is only known to the level of the differences in that figure.

Once more, we note that the Stokes visibilities are only the best guess at the true Stokes parameters. Without an exact characterization of the primary beam or dense  $u$ - $v$  sampling, one does not have the ability to fully correct for the leakages mentioned. Hence, it is imperative to inspect the Stokes  $I$  signal’s corruption.

## 2.2. The Delay Spectrum Approach

The delay-spectrum approach to measuring the 21cm power spectrum (Parsons et al. 2012b) requires no imaging, again providing an incentive for adding raw visibilities. The delay-spectrum approach embraces the natural units of an interferometer by sampling the power spectrum in baseline and frequency dimensions, native to an interferometer. With this approach, each baseline can be individually transformed into an estimator of the power spectrum of the incident temperature. This method also prevents the small-scale structure introduced by Fourier transforming over gain calibration errors (Morales et al. 2012).

Perhaps the greatest advantage of the delay spectrum approach is its ability to isolate smooth-spectrum foregrounds on a per-baseline basis. This relaxes the burden of isolating sources in the image plane, and allows for a more sparsely sampled array (e.g. a redundantly sampled one, as in Parsons et al. 2012a). The 21cm EoR’s extent to super-horizon delays depends precisely upon its spectral non-smoothness. It is imperative, then, to identify and characterize spectrally non-smooth foregrounds that may corrupt the EoR measurement.

The delay spectrum approach is particularly useful for simulating the effects of a systematic error on the power spectrum. Because each visibility estimates the power spectrum, a simulation needs only create one visibility, which encapsulates much of the power spectral information needed for analysis. The computational cost is additionally reduced by the ability to calculate a power spectrum by Fourier transforming only one visibility, rather than gridding several visibilities into a  $(u, v, \nu)$  cube and Fourier transforming along each  $u, v$  pixel.

It is important to note that the results of this paper

are not limited to delay-spectrum-based analyses. All effects mentioned in this paper are native to the sky and its expected spectral structure. Any analysis technique will incur all the same issues; we use the delay spectrum as a convenient probe for these issues.

We briefly review the definition of the delay transform as a Fourier transform over the frequency axis of a visibility:

$$\tilde{\mathcal{V}}(\tau) \equiv \int_{\Delta\nu} \mathcal{V}(u, v, \nu) e^{-2\pi i \tau \nu} d\nu, \quad (5)$$

where  $\nu$  represents the frequency,  $\tau$  is the delay or the Fourier transform pair to frequency, whose physical meaning is given in Parsons et al. (2012b), and the tilde denotes a delay-transformed visibility. We treat this as an estimator of the Fourier transform of the temperature field, squaring it to derive an estimator of the 3-D power spectrum  $P(\vec{k})$ ,

$$\tilde{\mathcal{V}}^2(\tau) = |\tilde{\mathcal{V}}(\tau)|^2 \propto P(\vec{k}). \quad (6)$$

where  $\vec{k}$  is the wavemode corresponding to the measurement. To better mimic actual measurements, we divide the band into ten, 6-MHz sub-bands, and perform the delay transform on each individual band. The sub-bandwidth is chosen to sample the maximum cosmological distance over which the 21cm signal is expected to be cotemporal (Wyithe & Loeb 2004; Furlanetto et al. 2006a, e.g.). Once these transforms are computed, we multiply each spectrum by the appropriate factors to obtain the power spectrum in units of temperature squared. We write the expression converting the squared, delay-transformed visibility  $\tilde{\mathcal{V}}(\tau)$  into a “unitless,” cosmological power spectrum  $\Delta^2(k)$  as

$$\tilde{\mathcal{V}}^2(\tau) \approx \left( \frac{2k_B}{\lambda^2} \right)^2 \frac{\Omega B}{X^2 Y} \frac{2\pi^2}{k^3} \Delta^2(k), \quad (7)$$

where  $k_B$  is the Boltzmann constant,  $\lambda$  is the observing wavelength,  $\Omega$  is the solid angle of the primary beam,  $B$  is the observed bandwidth, and  $X$  and  $Y$  are cosmological scalars which convert observed angles and frequencies in to  $h\text{Mpc}^{-1}$ , appropriately derived from Equations 3 and 4 of Furlanetto et al. (2006b).

Parsons et al. (2012b) offers a much more detailed discussion of this approach, beyond the scope of this paper.

## 2.3. Sparse $u$ - $v$ Sampling and Wide-Field Polarimetry

Another advantage of the delay spectrum approach is that it relaxes the requirement of gridding in the  $u$ - $v$  plane. Each baseline is assigned a position in the  $u$ - $v$  plane *ab initio*, and visibilities from similar baselines may be coherently added without imaging. This allows for sparse sampling in the  $u$ - $v$  plane without damaging effects from side lobes or missing data, problems other methods may experience. Since the delay spectrum rotates a power-spectrum estimate into the native coordinate system of an interferometer, there are no inherently missing frequency-data. Parsons et al. (2012a) presents the sensitivity benefits of a sparse, redundant array configuration, but other techniques aim to uniformly sample

the  $(u, v, \nu)$  cube, in order to mitigate the systematic effects of computing a Fourier Transform across unevenly sampled data.

An obvious disadvantage of having sparsely-sampled data is poor imaging. Not only does sparse sampling provide a highly irregular synthesized beam, but it also limits the available information for a full reconstruction of the image. Without adjacent  $u$ - $v$  samples, a full, accurate deconvolution by a wide beam simply has insufficient information. As we will see, the inability to correct for beam effects will provide a significant source of systematic error via polarized leakage.

By choosing to wield the full power of the delay spectrum approach and redundant sampling, an observer is forced to add visibilities with no beam weighting. The beam information supplied by adjacent  $u$ - $v$  samples simply does not exist, and without transforming into the image plane is unrecoverable. Hence, the imperative to investigate the implications of a lack of beam-weighting, the naïve construction of the  $I$  visibility, arises.

Together, redundant sampling and the delay spectrum approach give a 21cm EoR experiment incentive to add raw visibilities, subjecting it to potential leakage. An elliptical primary beam gives a mechanism whereby polarized emission can corrupt an estimate of the total power. To what degree does polarized emission corrupt an estimate of the 21cm EoR signal? We will begin answering this question by characterizing the spectral non-smoothness that will possibly arise from the rotation measure structure of polarized leakages.

#### 2.4. Faraday Rotation

Faraday Rotation affects the polarization properties of an electromagnetic wave traveling through a plasma containing a magnetic field (Rybicki & Lightman 1979). The circular polarization oriented in a right-handed fashion to the direction of the incident field will be slowed by the plasma. This causes a rotation of the E-field's polarization angle by

$$\Delta\phi = \lambda^2 \frac{e^3}{(m_e c^2)^2} \int B_{||}(s) n_e(s) ds \equiv \lambda^2 RM. \quad (8)$$

Equation 8 defines the rotation measure ( $RM$ ) by which we characterize this phase wrapping. Since the Stokes parameters characterize the square of the electric field, the phase of the polarization vector is shifted by twice the angle defined in equation 8. After a signal passes through a Faraday screen, we measure a rotated polarization angle,

$$(Q + iU)_{meas} = (Q + iU)_{int} e^{2iRM\lambda^2}, \quad (9)$$

where the subscript “meas” denotes the measured  $Q$  and  $U$  measurements, and “int” denotes the intrinsic  $Q$  and  $U$  signal, as would be measured behind the Faraday screen.

### 3. SIMULATION

#### 3.1. Single-Source Power Spectrum

We begin our investigation of the effects of polarized foregrounds on the 21cm EoR signature by examining the power spectrum of a single source at zenith, whose signal has the structure of a single  $RM$ . In doing so, we

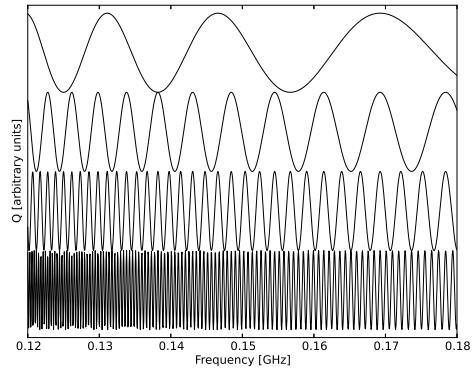


FIG. 3.— Real component of the visibility  $\mathcal{V} = \exp\{-2RM\lambda^2\}$  for rotation measures 3, 10, 30 and  $100 m^{-2}$ , from top to bottom. This plot is intended to demonstrate both the frequency-dependent phase wrapping and the frequency-dependent critical sampling of Faraday rotation. Notice how the  $100 m^{-2}$  component (located at the bottom) is critically sampled at high frequencies, but loses coherence at low frequencies.

can develop an intuition for the rotation measures that affect cosmologically interesting  $k$  modes of the power spectrum. By looking at what is effectively the impulse response of a Faraday screen on the power spectrum, it will be easier later to interpret a more complicated model.

Figure 3 shows the real part of the spectra of a few linearly polarized sources behind Faraday screens,  $S(\nu) = \exp\{-2iRM\lambda^2\}$ . Each spectrum contains one source with one-Jansky of polarized flux, located at zenith (delay of zero). Notice that at the highest rotation measure shown, the spectrum is not critically sampled at the lowest frequencies. This is due to the uneven sampling of  $\lambda^2$  across the band: as  $\Delta\lambda^2 \approx d\lambda^2/d\nu \Delta\nu \propto \Delta\nu/\nu^3$  increases, the sensitivity to large rotation measures decreases.

Figure 4 shows the Fourier transform over frequency of the spectra in Figure 3. While this doesn't exactly represent the delay-spectrum of a visibility — there is no beam-weighting, and no  $\exp\{-2\pi i \vec{b} \cdot \vec{s}\}$  component, which essentially defines the delay spectrum — we interpret it as the delay-structure introduced by a polarized source behind a Faraday screen. The results of these transforms over the full simulated band are shown in figure 5. The most important feature of this plot is this: there is a  $k$  mode associated with each rotation measure at each redshift. We can construct an analytic estimate of this  $k$  mode by setting the argument of the exponents of a delay mode and a rotation measure mode to sum to zero. First, we approximate the cosmological  $k$ -mode sampled by a delay mode as  $\tau \approx k_{||} dr_{||}/d\nu$ . Next, we recall the cosmological scaling from frequency into  $h\text{Mpc}^{-1}$ ,

$$\frac{dr_{||}}{d\nu} = \frac{dr_{||}}{dz} \frac{dz}{d\nu} = -\frac{c(1+z)}{H(z)\nu}. \quad (10)$$

Finally, we set  $k_{||} \cdot dr_{||}/d\nu \cdot \nu + 2RM\lambda^2 = 0$ . Substituting Equation 10 for the derivative, we derive an expression for the  $k$ -mode most affected by a rotation measure  $RM$ :

$$k_{||} \approx \frac{2}{c} \frac{H(z)}{1+z} \cdot RM\lambda^2, \quad (11)$$

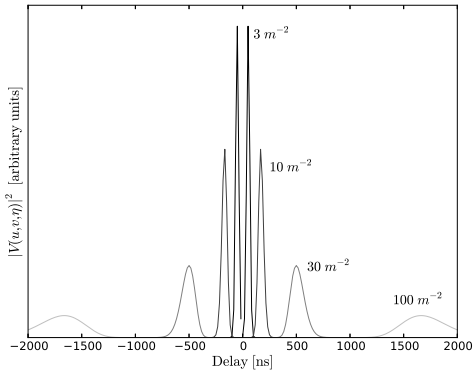


FIG. 4.— Delay spectra of the Faraday-screened visibilities shown in figure 3. This plot demonstrates the effect of a Faraday screen on the delay spectrum of a source. There are two effects: first, a Faraday screen widens the response of a spectrum in delay space, and second, the Faraday screen scatters power to high delay. This causes a potential problem as many foreground removal techniques require smooth-spectrum foregrounds. Note that higher rotation measures mimic higher delays.

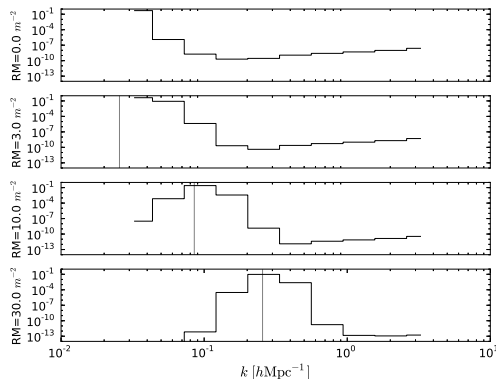


FIG. 5.— Power spectra of the visibilities plotted in Figure 3, computed for the median redshift bin of the PAPER band ( $z \sim 8$ ). This plot demonstrates the coupling between rotation measure and  $k$ -modes, and confirms that Faraday-rotated spectra scatter power to higher  $k$  modes than would be contained within the horizon. Grey, vertical lines show the maximally-infected  $k$ -mode, predicted by equation 11. The rise in power at high  $k$  is due to the  $\sim 10^{-9}$  sidelobe of the Blackman-Harris filter. The units of the y-axis are tuned so the total power integrates to one.

where  $H(z)$  is the Hubble parameter. Figure 6 shows a plot of the most culpable rotation measure versus frequency and redshift.

### 3.2. Full-Sky Simulation

To better grasp the effects of Faraday leakage into the 21cm signal, we generate several random realizations of the sky, each consisting of many polarized point sources. Each source passes through a Faraday screen with some rotation measure, chosen from a distribution based on current measurements. Next, we simulate that source for a single baseline. Finally, we calculate the power spectrum measured by that visibility. Only one visibility needs to be simulated, because the delay-spectrum approach makes use of the fact that each baseline measures the 21cm EoR with a range of  $k$ -modes determined by the baseline length, orientation, and bandwidth.

As mentioned before, we use PAPER as a model for

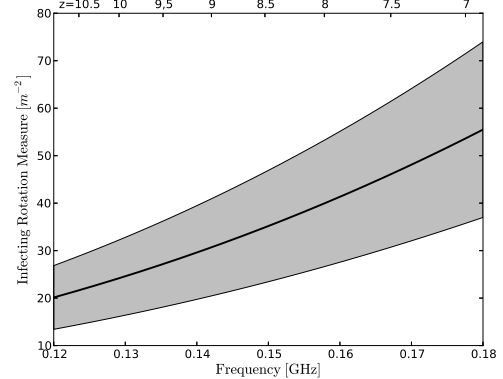


FIG. 6.— The rotation measure most affecting  $k \approx 0.15 \text{ hMpc}^{-1}$ , calculated from equation 11. Shaded region indicates the range of rotation measures affecting  $0.1 \lesssim k \lesssim 0.2 \text{ hMpc}^{-1}$ .

choosing instrumental parameters. Our simulated band goes from 120 to 180 MHz, with 60 kHz channels. We use a simulated primary beam model of the PAPER dipole, which has a full width at half max of around  $45^\circ$  at 150 MHz (Pober et al. 2012).

Rather than creating an exact simulation of the physical sky, we create a simulation whose statistical properties are physically motivated. This choice reflects a desire for simple, easily tunable parameters for the simulation. In that same spirit, we model all sources simply as point sources with a Poisson distribution. The simulation’s primary concern with the spectral information of polarized foregrounds allows us to justify neglecting the angular terms. This is equivalent to assuming for all the relevant  $k$  modes,  $k_{\parallel} \gg k_{\perp}$ . Emphasis on the  $k_{\parallel}$  or spectral modes also motivates our decision to model the sky as numerous point sources. For a more detailed discussion of these effects, we direct the reader to Jelić et al. (2010).

Source positions are distributed uniformly over the sphere. A single source’s altitude  $\theta$  is drawn from a distribution in which  $\cos \theta$  is uniform on  $[0, 1]$ . A source’s azimuthal angle  $\phi$  is drawn independently from  $\cos \theta$  from a distribution uniform on  $[0, 2\pi]$ . This choice of source position distributions conserves the density per area of sources across the sky, and is equivalent to drawing both direction cosines,  $(l, m) = (\sin \theta \cos \phi, \sin \theta \sin \phi)$ , from a uniform distribution on  $[-1, 1]$ .

In order to achieve realistic source fluxes and source counts, we base the distributions from which we draw various parameters on previous radio surveys. For the source fluxes, we aim to agree with VLSS (Cohen et al. 2007), NVSS surveys (Condon et al. 1998), and the 6C survey (Hales et al. 1988). For the polarization information, we aim to agree with polarized measurements taken by the NVSS survey, particularly, their nearly full sky rotation measure map (Taylor et al. 2009), as well as the polarized survey of the VLSS.

We present two scenarios for the source counts. First, we draw from the 6C distribution (Hales et al. 1988), taken in the PAPER band at 151MHz. Second, we extrapolate VLSS source counts (Cohen et al. 2007) from 74 MHz to 150 MHz, using a spectral index of -0.79, following the work of Cohen et al. (2004). The latter source counts provide more sources at higher flux, which infect

the power spectrum from the  $I$  visibilities, as we will show in the following sections. Both number counts are consistent with the recent measurements by the Murchison Widefield Array (Williams et al. 2012), an instrument similar in many regards to PAPER.

The differential number counts ( $dN/dS$ ) found by Hales et al. (1988) may be characterized by two power laws, turning over at some knee flux  $S_o$

$$\frac{dN}{dS} = \begin{cases} 4000 S_o^{-0.76} S^{-1.75} Jy^{-1} sr^{-1} & S_{min} \leq S < S_o \\ 4000 S^{-2.81} Jy^{-1} sr^{-1} & S_o \leq S \end{cases} \quad (12)$$

Following the 6C survey, we choose the turning point,  $S_o$  to be 0.88 Jy. The number of sources simulated (14,855) is chosen by the size of the PAPER beam at 151 MHz (0.76 sr) and a flux range over which to integrate. We choose to include those sources in between 100 mJy and 10 Jy. This choice provides a reasonable dynamic range of sources. Below the lower limit, the 6C sources are unreliable, and we assume sources above 10 Jy may be easily identified and removed.

If we were to blindly extrapolate the 6C source counts below the lower limit of the catalog, we would add a negligible amount of power. Integrating  $S^2 dN/dS$  down to some minimum flux estimates the contribution of the sources above that flux to the total variance of flux. By inserting the 6C source counts, we find that we are including  $\sim 70\%$  of the estimated total variance. Extending the minimum flux would add more power to the simulation, but would not drastically alter the results of this paper.

VLSS source counts follow a single power law, given by Cohen et al. (2004) as

$$\frac{dN}{dS} = 4865 S^{-2.3} Jy^{-1} sr^{-1}. \quad (13)$$

For these source counts, we choose minimum and maximum fluxes of 0.8 Jy and 100 Jy, respectively, rejecting sources well below the lower limit of the catalogue, and providing a reasonable dynamic range for the included sources. Integrating over the PAPER beam provides 6995 sources. These source counts are not qualitatively different from the 6C counts at low fluxes, but they do differ substantially in that they provide many more bright sources.

For both source counts, we also assign a spectral index to each individual source spectrum, drawn from a normal distribution, mean -0.8, standard deviation 0.1, which roughly agrees with the findings of Helmboldt et al. (2008).

Each source is also assigned a random polarization angle  $\chi$ , uniformly sampled from  $[0, \pi]$ . Total flux is multiplied by a polarization fraction, chosen to reflect the studies of Tucci & Toffolatti (2012). We sample the polarized fraction ( $\Pi$ ) from a log-normal distribution whose mean is 2.01% and whose standard deviation is 3.84%. Because the log-normal distribution is not upper-bounded, we reject any drawing over 30%. Following the aforementioned study, we do not impose any correlation between source flux and polarization fraction. It has been noted that, among other effects, bandwidth depolarization causes the polarized fraction to decrease at lower frequencies (Law et al. 2011). This along with

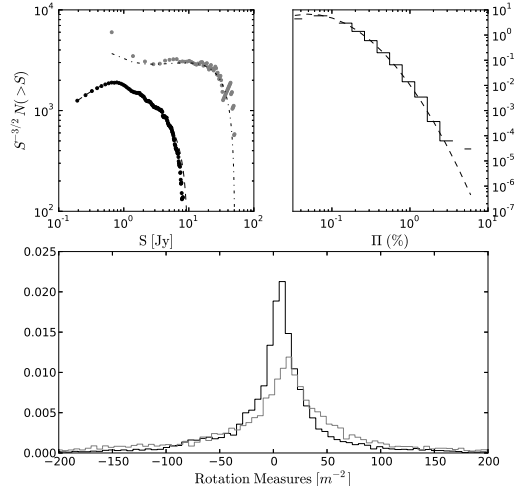


FIG. 7.— Distributions of simulated parameters. (Top Left)  $S^{-3/2}N(>S)$  source counts of unpolarized flux. In black, the 6C source counts, from Hales et al. (1988), and in grey, the VLSS counts, from Cohen et al. (2007). (Top Right) Normalized histogram of the log-normal distribution of polarized fraction, taken from Tucci & Toffolatti (2012). (Bottom) Normalized histograms of the two distributions of rotation measures. Black is taken from Oppermann et al. (2012), grey is that with a doubled standard deviation. The  $RM$  distribution extends to several hundred  $m^2$ , but we restrict the extent of the  $x$ -axis to highlight the distribution, rather than the width of its tails. In the upper two panels, the dashed line is the distribution from which sources are drawn, and the bins or points are the values of one realization of the simulation.

measurements from Pen et al. (2009) indicates that these distributions, taken at 1.4 GHz, may overestimate the distribution at 150 MHz. We neglect these effects, taking the 1.4 GHz distribution at face value, since the mean polarization fraction can be thought of as a scale factor to the overall power spectrum.

We base our distribution of rotation measures on the map presented in Oppermann et al. (2012). To mimic the effects of depolarization due to a finite spatial resolution (Law et al. 2011, e.g.), we apply a low-pass filter to the  $RM$  map. We project the map into a spherical-harmonic basis, and keep only those modes below the resolution of our simulated instrument. In the case of this simulation, we choose to keep only  $\ell \leq 100 = 2\pi|u|$ . This averages the polarization vectors in much the same way as a synthesized beam, and its effect is to essentially remove outliers in the  $RM$  distribution, to which instruments like PAPER may not be sensitive. We then randomly draw rotation measures from the computed cumulative distribution function of  $RM$ 's given in the Oppermann et al. (2012) data. Aside from low-pass filtering, no spatial information from the data is used. Section 3.4 briefly discusses the negligible consequences of spatially correlating  $RM$ .

Histograms of the distributions of rotation measure, polarized fraction, and source counts can be found in figure 7. Over-plotted on all is the distribution from which they are drawn.

We model all sources as point sources, neglecting the effects of any diffuse emission. This choice reflects the desire for a simple, easily tunable parameters in the simulation. While diffuse emission certainly is present, its

Name	Source Counts	$N_{src}$	$RM$ distribution
A	6C	14,855	Oppermann
B	VLSS	6,995	Oppermann
C	6C	14,855	$2 \times$ Oppermann

TABLE 1  
SIMULATION TREATMENTS

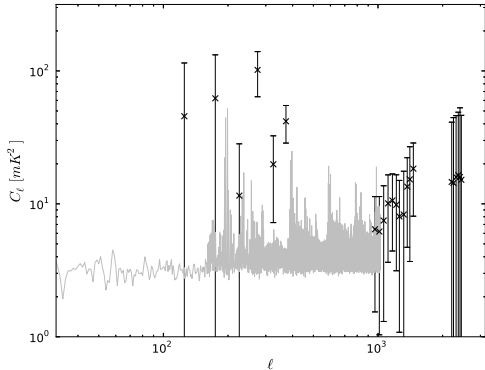


FIG. 8.—  $\ell$  vs.  $C_\ell$  for one realization of the simulation (solid line), alongside the results from Bernardi et al. (2010), (crosses). This roughly demonstrates the agreement of the simulation presented in section 3.2 with current observations. The simulation is consistently lower than the observed values due to the lack of extended structure.

spectral structure is qualitatively the same as that of a point source, so the results in the frequency direction will not change. Were we to add a diffuse model to the simulation, it would widen a source’s response in delay-space, preventing it from being localized. This will not affect the line-of-sight power spectrum, at high  $k$ , since the spectrally-smooth, diffuse emission still falls within the horizon.

Table 1 summarizes the three treatments of the simulation we will be using. Simulation A, with 6C source counts and the Oppermann  $RM$  distribution is likely the most accurate. Simulation B steepens the source counts, providing fewer, brighter sources, and simulation C doubles the width of the  $RM$  distribution.

To check if the results of this simulation are consistent with the measurements in Bernardi et al. (2010), we compare the two-dimensional  $C_\ell$  power spectrum with that presented in their paper. Figure 8 shows the 2D power spectrum of one realization of the simulation, with the constraints from figure 20 of Bernardi et al. (2010) plotted over it. We see qualitatively that our simulation well obeys the upper-limit imposed by the Bernardi measurement, and proceed with the results.

We calculate the visibilities for a 32m, east-west baseline. This choice reflects the most common spacing of the maximum-redundancy configuration presented in Parsons et al. (2012a). The choice of baseline orientation is arbitrary, and since we are modeling only point sources, the choice of baseline length will only set the horizon limit of the power spectrum. Since the delay affected by a rotation measure is independent of a choice of baseline (equation 11), choosing a relatively short baseline will isolate the foregrounds at lower  $\tau$ , and highlight the Faraday leakage.

The full measurement equation used in this simulation

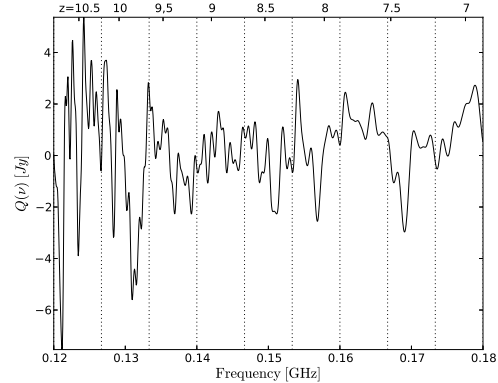


FIG. 9.— Simulated  $Q$  visibility with the parameters shown in figure 7.

is

$$\mathcal{V}(u, v, \nu) = \sum_{j=1}^{N_{src}} A(l_j, m_j, \nu) \Pi_j S_j^{150} \left( \frac{150 \text{ MHz}}{\nu} \right)^{\alpha_j} \times \exp \left\{ -i[2\pi\nu(ul_j + vm_j) + 2RM_j\lambda^2 + 2\chi_j] \right\}, \quad (14)$$

where each source  $j$  is assigned a flux ( $S_j$ ), polarization fraction ( $\Pi_j$ ), spectral index ( $\alpha_j$ ), a position ( $l_j, m_j$ ), rotation measure ( $RM$ ), polarization angle ( $\chi_j$ ), and is weighted by the model primary beam ( $A$ ). A sample  $Q$  visibility is shown in Figure 9.

We choose not to include the parallactic rotation of  $Q$  into  $U$ , implying that the  $Q$  we label in this paper are fixed to topocentric, azimuth and altitude coordinates. This choice clarifies equations and allows for an ease of understanding which would be obfuscated by writing both  $Q$  and  $U$ .

### 3.3. Simulated Power Spectra

Figure 10 show the power spectra for source counts from the extrapolated VLSS and 6C surveys, as well as the spectrum of 6C source counts with a widened rotation measure distribution. We interpret the power spectrum of the  $I$  visibility as the amount of polarized leakage corrupting the EoR signal (henceforth called  $Q \rightarrow I$  leakage), and the  $Q$  visibility’s power spectrum is our best representation of the polarized signal. These plots show the median power in each  $k$  bin for 1000 realizations of the simulation, with error bars show the one-sigma extent of the bandpowers for these realizations. These power spectra confirm the prediction of section 3.1, that  $\lambda^2$  phase wrapping extends the foreground cut-off presented in Parsons et al. (2012b) to higher  $\tau$  bins, corrupting some of the most sensitive regions of  $k$  space for 21cm EoR analysis. They also demonstrate the prediction in that section that high-redshift bins will be most affected.

The severity of the leakage can be inferred from the power in the most EoR-sensitive  $k$  bins ( $0.2 \text{ hMpc}^{-1} \lesssim k \lesssim 0.3 \text{ hMpc}^{-1}$ ). Figure 11 shows  $\Delta^2(k)$  in these bins as a function of redshift. The leaked power ranges in the thousands of  $\text{mK}^2$ , increasing from high frequency / low redshift to low frequency / high redshift. These estimates are about two orders of magnitude above level

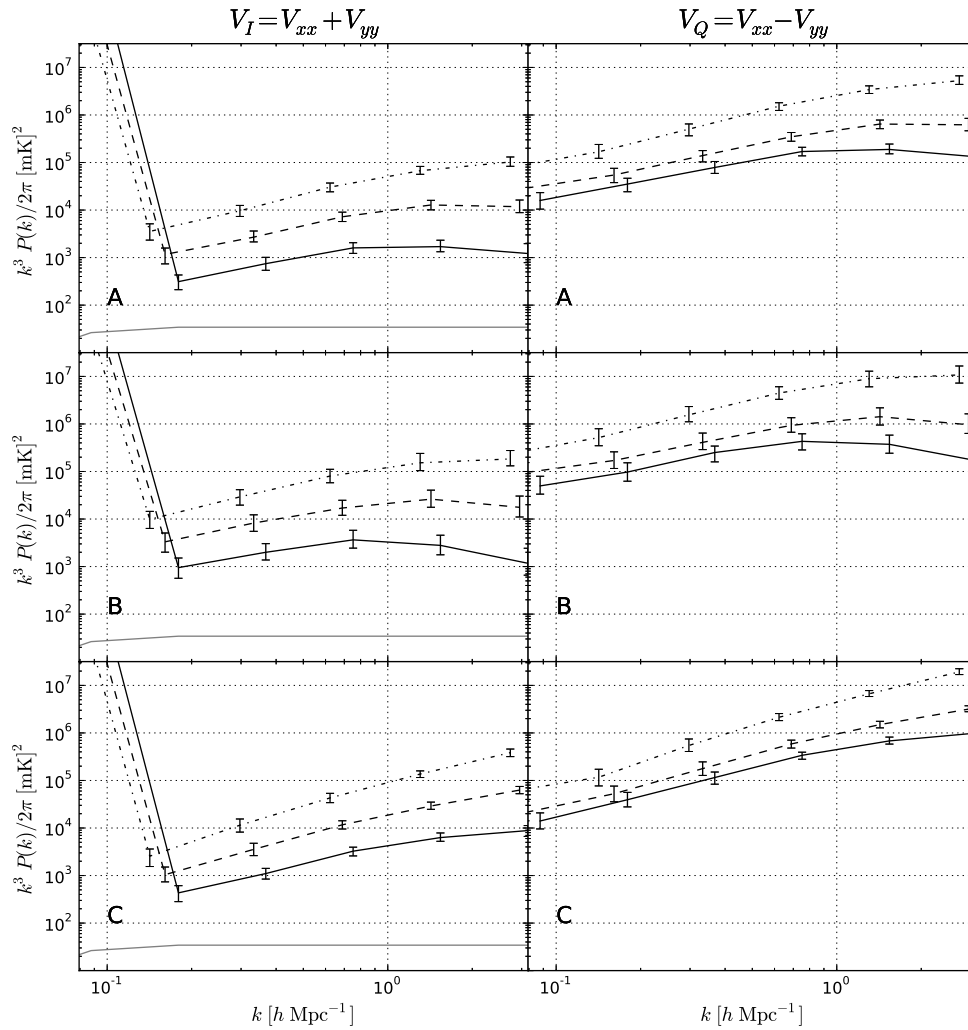


FIG. 10.— Power spectral measurements for the three treatments of the simulation shown in Table 1. The left column shows the power spectra of the  $I$  visibilities, and the right shows the spectra of  $Q$  visibilities. The top row shows simulation treatment A, the second row shows treatment B, and the third row shows treatment C. Line styles depict different redshift bins: 7.25 (solid), 8.33 (dashed), 9.73 (dot-dashed). Grey line give a toy model of the expected 21cm emission from Furlanetto et al. (2006b). Both visibilities include contributions from both the (intrinsic) Stokes  $I$  and  $Q$ . The simulated levels of  $Q$  emission indicate that polarized leakage into  $I$  needs to be less than for or five orders of magnitude in  $\text{mK}^2$ .

of the expected 21cm signal (Lidz et al. 2008). If we take this simulation as an accurate prediction of the low-frequency sky’s polarized emission, these results imply that naïvely adding  $\mathcal{V}_{xx}$  and  $\mathcal{V}_{yy}$ , formed with an approximately 10% asymmetric primary beam, incorporates enough bias from polarized leakage to completely obscure the 21cm signal. The levels of leakage in our simulations demands a strategy to model and remove polarized sources.

We note that simply adding  $\mathcal{V}_{xx}$  and  $\mathcal{V}_{yy}$  will also remove a negligible component of the EoR signal via the same mechanism. In a sense,  $Q \rightarrow I$  leakage can be thought of as a rotation of power between the two Stokes parameters. Hence, for precision measurements of the EoR signal, this simple estimate may not be ideal. However, the effect of  $I \rightarrow Q$  leakage is small (compare the

levels of  $\mathcal{V}_Q$  and high- $k$  modes of  $\mathcal{V}_I$ ) and should not provide a significant hindrance to detection.

### 3.4. Correlated Polarization Vectors

The results of the previous section were intended to extrapolate previous measurements to low fluxes and investigate the effects of an unresolved forest of dim, polarized point sources. It neglects the known spatial correlations of the rotation measure distribution (Kronberg & Newton-McGee 2011). Furthermore, the random drawing of polarization angle could have a cancelling effect on the visibilities. This neglect could potentially suppress our estimation of polarized leakage into the power spectrum.

To investigate the possible effects of correlating the polarization vector, we include a treatment of the simu-

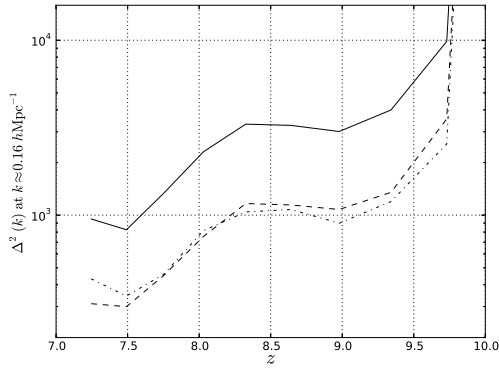


FIG. 11.— Median  $Q \rightarrow I$  leakage for the  $k \approx 0.16 h\text{Mpc}^{-1}$  bin of the power spectrum,  $\Delta^2(k)$  vs.  $z$  for all treatments of the simulation shown in figure 10, and defined in table 1: A (solid), B (dashed), C (dot-dashed). We note that with every treatment, the amount of polarized flux leaking into the power spectrum grows with  $z$ , confirming that leakage is worse at lower frequencies.

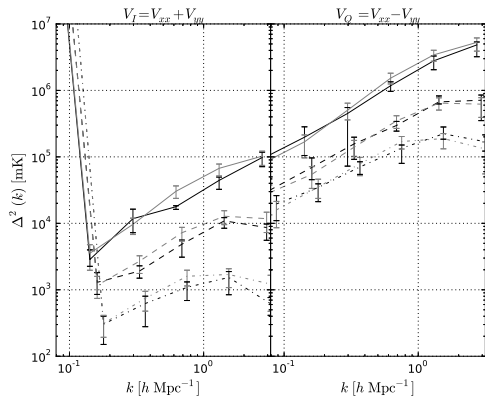


FIG. 12.— A comparison of power spectral measurements for a treatment of the simulation with correlated polarization angles (black), and those with treatment A from Table 1 (gray). As in figure 10, the left-hand panel shows the power spectrum derived from the  $I$ -visibility, and the right-hand panel, the  $Q$ -visibility. Three redshift-bins are included, and denoted by linestyles: 9.73 (solid), 8.33 (dashed), and 7.25 (dot-dashed). The results of simulation A agree with the results of correlating polarization vectors, which indicates that our choice of randomly-assigning polarization angles and rotation measures is valid.

lation where we choose rotation measures from the Oppermann map (Oppermann et al. 2012), with a pointing center at the Galactic south pole — a reasonable field for EoR analysis. We then set all polarization angles to zero, maximally correlating polarization vectors, while still including information of the polarized sky. All other simulation parameters are identical to simulation A of Table 1. Figure 12 compares the results of this treatment with simulation A of the previous section. The power spectrum of this treatment agrees with simulation A at all redshifts and values of  $k$ , for both polarizations. This agreement indicates that spatial correlations in  $RM$  and polarization angle do not significantly affect polarized leakage into the power spectrum. Thus the assumption of the previous section that the polarization vectors are spatially uncorrelated does not affect the results of this paper.

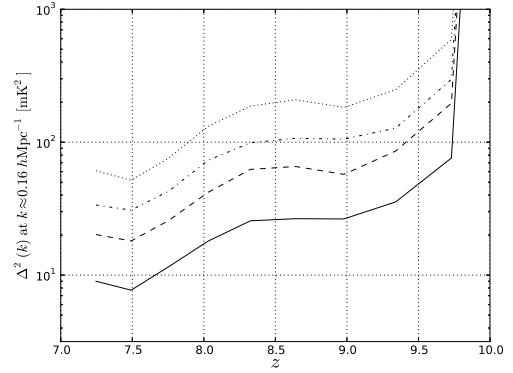


FIG. 13.—  $\Delta^2(k)$  vs  $z$  at a single  $k \approx 0.16 h\text{Mpc}^{-1}$ . Each line style shows the volume-averaged power after the brightest  $N$  sources were removed from the simulation. The number of removed sources,  $N$  is depicted by line style. Dotted: 1000 sources removed (40 mJy), dot-dashed; 2000 removed (25 mJy), dashed; 3000 removed (18 mJy), and solid: 5000 removed (11 mJy).

#### 4. MITIGATION

Section 3 predicts an excess polarized signal due only to point sources at around  $10^4 \text{ mK}^2$  at  $k \sim 0.15$  for most treatments of the simulation. While the exact levels of these predictions may be subject to some error, the need certainly arises for some removal scheme, which must roughly suppress power from polarized foregrounds by around four orders of magnitude in the power spectrum.

To investigate the effects of modelling and removing polarized sources, we rerun the simulation, excluding the brightest polarized sources. Figure 13 shows the median value of 500 simulations of one  $k$ -bin of the power spectrum for removing the brightest 1000, 2000, 3000, and 5000 sources. These limits in number of sources correspond to flux-limits of 40 mJy, 25 mJy, 18 mJy, and 11 mJy, respectively. We remove these sources from treatment A of the simulation, which includes around fifteen thousand sources. Despite having removed nearly one-third of the sources, the leaked power still exceeds  $10 \text{ mK}^2$ .

To remove enough flux to consistently fall below the expected EoR signal, we needed to remove eight to ten thousand sources ( $\sim 6 \text{ mJy}$ ), roughly the number of sources in the simulation. We recomputed these fluxes with a lower minimum flux (60 mJy), expecting a similar result, but found that we increased the power in this  $k$ -bin by one or two  $\text{mK}^2$ . Ten to twelve thousand sources required removal for the total power to fall below  $10 \text{ mK}^2$ . We exclude further investigation of this analysis for three reasons. First, current measurements do not constrain  $dN/dS$  to the levels necessary to accurately model such low-flux sources. Second, including lower-flux sources does not significantly affect the result that the expected polarized power spectrum will be of the order of  $10^4$ – $10^6 \text{ mK}^2$ . Third, the variance from one simulation to the next in the power was large enough that the two treatments of the simulation — even with ten thousand sources removed — could not be considered significantly different.

These onerous levels of source-removal suggest that a different mitigation scheme be considered. Future instruments may take polarization into consideration in

design. Leakage can be mitigated with more circular beams, and circular feeds avoid  $Q \rightarrow I$  leakage entirely. Even with existing data, rotation measure synthesis (Brentjens & de Bruyn 2005) could potentially provide the power to separate sources with distinct  $RM$  structure to be separated from EoR signal.

## 5. DISCUSSION

Were a power spectrum computed from only one linearly polarized visibility ( $xx$ , for instance), all polarized power would corrupt the measurement. We have chosen to suppress the polarized leakage by adding linearly-polarized visibilities. The leakage is dependent on the difference of the two beams, and by having beams that are at most ten percent different suppresses the signal by around two to three orders of magnitude. Correcting for the beam-weighting in the image domain can further suppress the leakage, but errors in the beam model will introduce leakage in much the same manner. Hence, the constraint of having to suppress polarized leakage by four orders of magnitude causes the need for an accurate primary beam model to around the one percent level in the case of imaging, or symmetric at the one percent level if visibilities are used directly.

These estimates of power are also dependent on the relative strengths of diffuse, polarized emission and polarized point sources. We have taken care to agree with current measurements, but we note that above  $\ell \sim 300$ , the current constraints are noisy. We have interpreted them as an upper limit. In the limiting case where diffuse emission is the only component to the polarized sky, this leakage could be suppressed by measuring with a longer baseline, which in turn measures lower  $\ell$  and  $k_{\perp}$ . We have chosen to use a sixteen-wavelength baseline, which corresponds to  $\ell \approx 200$ . This choice of baseline length is relatively short for interferometers at these wavelengths, but falls at the high end of the Bernardi et al. (2010) detection.

Including diffuse emission in the simulation would certainly increase the total power in the simulation for low  $\ell$ , but the frequency structure would remain qualitatively the same as point sources. As we showed in Section 3.4, the correlation of rotation measure and polarization angle that could be introduced by an extended structure does not significantly affect the power spectrum. For this reason, we can consider the polarized sky as having two

components with nearly identical footprints in the power spectrum: diffuse and point like. Both components will exhibit similar frequency structure, so choice of baseline length will set the relative weightings of these components. Bernardi et al. (2010) briefly discuss some of the implications of their measurement of extended structure to the three-dimensional power spectrum in their conclusion, which agrees with our analysis of point-like structure.

We conclude our discussion of the simulation results by noting the large variance in the simulated power. The results shown are the median band-powers in  $\Delta^2(k)$  for 500 realizations of the simulation. Taking so many realizations into account essentially maps out the posterior distribution of the  $\Delta^2(k)$  bandpowers. The one-sigma width covers nearly an order of magnitude, which indicates the level of Faraday leakage is highly sensitive to the exact parameters drawn in any realization. The actual level of leakage measured will thus be highly dependent on a choice of field, and on cosmic variance.

## 6. CONCLUSION

We have predicted the three-dimensional power spectrum of polarized emission around 150 MHz to be in the range of  $10^4$ - $10^6$  mK<sup>2</sup> at  $k_{\parallel} \sim 0.15$  hMpc<sup>-1</sup>. These predictions were based on simulations motivated by current observations of the polarized sky at 150 MHz and 1.4 GHz. An elliptical beam provides one mechanism for this power to leak into a measurement of the unpolarized signal. Using a fiducial model of the PAPER beam, we estimated this leakage to be in the thousands of mK<sup>2</sup>, several orders of magnitude above the expected 21cm EoR signal. Modelling and removing polarized sources may eliminate much of this leakage, but these simulations suggest the amount of removal required far exceeds reasonable capabilities of current instruments.

Work is currently underway to measure frequency structure of polarized power, to investigate the amount of its leakage into the  $I$  power spectrum, and to better characterize the polarized radio sky using existing PAPER data.

This analysis and the PAPER project are supported through the NSF-AST program (award 1129258). Computing resources were provided by a grant from Mt. Cuba Astronomical Foundation.

## REFERENCES

- Bernardi, G. et al. 2010, A&A, 522, A67  
 Bowman, J. D., Morales, M. F., & Hewitt, J. N. 2009, ApJ, 695, 183  
 Brentjens, M. A. & de Bruyn, A. G. 2005, A&A, 441, 1217  
 Cohen, A. S., Lane, W. M., Cotton, W. D., Kassim, N. E., Lazio, T. J. W., Perley, R. A., Condon, J. J., & Erickson, W. C. 2007, AJ, 134, 1245  
 Cohen, A. S., Röttgering, H. J. A., Jarvis, M. J., Kassim, N. E., & Lazio, T. J. W. 2004, ApJS, 150, 417  
 Condon, J. J., Cotton, W. D., Greisen, E. W., Yin, Q. F., Perley, R. A., Taylor, G. B., & Broderick, J. J. 1998, AJ, 115, 1693  
 Dillon, J. S., Liu, A., & Tegmark, M. 2013, Phys. Rev. D, 87, 043005  
 Furlanetto, S. R., McQuinn, M., & Hernquist, L. 2006a, MNRAS, 365, 115  
 Furlanetto, S. R., Oh, S. P., & Briggs, F. H. 2006b, Phys. Rep., 433, 181  
 Geil, P. M., Gaensler, B. M., & Wyithe, J. S. B. 2011, MNRAS, 418, 516  
 Hales, S. E. G., Baldwin, J. E., & Warner, P. J. 1988, MNRAS, 234, 919  
 Hamaker, J. P., Bregman, J. D., & Sault, R. J. 1996, A&AS, 117, 137  
 Haslam, C. G. T., Salter, C. J., Stoffel, H., & Wilson, W. E. 1982, A&AS, 47, 1  
 Heald, G., Braun, R., & Edmonds, R. 2009, A&A, 503, 409  
 Helmboldt, J. F., Kassim, N. E., Cohen, A. S., Lane, W. M., & Lazio, T. J. 2008, ApJS, 174, 313  
 Jelić, V., Zaroubi, S., Labropoulos, P., Bernardi, G., de Bruyn, A. G., & Koopmans, L. V. E. 2010, MNRAS, 409, 1647  
 Kronberg, P. P. & Newton-McGee, K. J. 2011, PASA, 28, 171  
 Law, C. J. et al. 2011, ApJ, 728, 57  
 Lidz, A., Zahn, O., McQuinn, M., Zaldarriaga, M., & Hernquist, L. 2008, ApJ, 680, 962  
 Liu, A. & Tegmark, M. 2011, Phys. Rev. D, 83, 103006  
 Liu, A., Tegmark, M., & Zaldarriaga, M. 2009, MNRAS, 394, 1575  
 Morales, M. F., Bowman, J. D., & Hewitt, J. N. 2006, ApJ, 648, 767

- Morales, M. F., Hazelton, B., Sullivan, I., & Beardsley, A. 2012, *ApJ*, 752, 137
- Oppermann, N. et al. 2012, *A&A*, 542, A93
- Parsons, A., Pober, J., McQuinn, M., Jacobs, D., & Aguirre, J. 2012a, *ApJ*, 753, 81
- Parsons, A. R. et al. 2010, 139, 1468
- Parsons, A. R., Pober, J. C., Aguirre, J. E., Carilli, C. L., Jacobs, D. C., & Moore, D. F. 2012b, *ApJ*, 756, 165
- Pen, U. L., Chang, T. C., Hirata, C. M., Peterson, J. B., Roy, J., Gupta, Y., Odegova, J., & Sigurdson, K. 2009, *MNRAS*, 399, 181
- Poher, J. C. et al. 2012, *AJ*, 143, 53
- Röttgering, H. 2003, *NAR*, 47, 405
- Rybicki, G. B. & Lightman, A. P. 1979, *Radiative processes in astrophysics*
- Taylor, A. R., Stil, J. M., & Sunstrum, C. 2009, *ApJ*, 702, 1230
- Tingay, S. J. et al. 2013, *PASA*, 30, 7
- Tucci, M. & Toffolatti, L. 2012, *Advances in Astronomy*, 2012
- Williams, C. L. et al. 2012, *ApJ*, 755, 47
- Wyithe, J. S. B. & Loeb, A. 2004, *Nature*, 432, 194